View metadata, citation and similar papers at core.ac.uk

brought to you by CORE

provided by Kyutacar : Kyushu Institute of Technology Academic Repository

九州工業大学学術機関リポジトリ
Kyutacar
Kyushu Institute of Technology Academic Repository

Relationship between Microstructure and Magnetic Domain Structure of Nd-Fe-B Melt-Spun Ribbon Magnets

著者	Takezawa Masaaki, Taneda Hiroyuki, Morimoto Yuji
journal or publication title	Frontiers of Materials Science
volume	9
number	2
page range	206-210
year	2015-06
URL	http://hdl.handle.net/10228/5683

doi: info:doi/10.1007/s11706-015-0297-5

Relationship between microstructure and magnetic domain structure of Nd–Fe–B melt-spun ribbon magnets

Masaaki Takezawa [a)], Hiroyuki Taneda, and Yuji Morimoto

Department of Applied Science for Integrated System Engineering, Faculty of Engineering, Kyushu Institute of Technology, 1-1 Sensui-cho, Tobata-ku, Kitakyushu, Fukuoka 804-8550, Japan

[a)] Tel.: +81-93-884-3236. Electronic mail: take@ele.kyutech.ac.jp

ABSTRACT

The relation between the microstructure, observed using an electron probe microanalyzer, and the domain structure, observed using a Kerr microscope, was established to evaluate the effects of hot rolling and the addition of Ti–C on the c-axis orientation and the magnetization process of hot-rolled Nd–Fe–B–Ti–C melt-spun ribbons. The addition of Ti–C promotes the c-axis orientation and high coercivity in the ribbons. Elemental mapping suggests a uniform elemental distribution; however, an uneven distribution of Ti was observed in an enlarged grain with Ti-enriched points inside the grain. The reversal domains that nucleated at the Ti-enriched point inside the grain cause low coercivity.

Keywords: magnetic domain, microstructure, Kerr effect microscope, magneto-optical effect, Nd–Fe–B permanent magnet,

1. Introduction

Nd-Fe-B permanent magnets are key materials for realizing energy-efficient motor for electrical vehicles. Because thermal stability up to 200 °C is required for electrical vehicles, a very high coercivity of 30 kOe at room temperature is necessary. Therefore, to enhance coercivity, commercially available Nd–Fe–B magnets containing a large amount of the minor metal Dysprosium (Dy) are used [1, 2]. However, the low natural abundance of Dy is a crucial resource problem. It is important for the problem to establish the coercivity mechanism of Nd-Fe-B magnet through microstructure observation. There are many reports about the relation between the coercivity and microstructure of Nd–Fe–B magnets [3-7]. In addition, it is important to clarify the relation between the microstructure and the domain structure of the magnet. In this study, we performed an elemental mapping analysis of Nd–Fe–B magnets by field emission-electron probe microanalyzer (FE-EPMA), and the relationships between the microstructure and the domain structure observed using a Kerr microscope were established to evaluate the effects of the microstructure on the magnetization process of Nd–Fe–B magnets.

As an observed sample, we fabricated hot-rolled Nd–Fe–B–Ti–C melt-spun ribbons having small coercivity. Hot rolling, a similar mechanism to die upsetting, [8] has been

reported to be used to fabricate c-axis-oriented Nd–Fe–B magnets. [9-11] However, the coercivity of hot-rolled Nd–Fe–B ribbons is small because of the growth of columnar grains owing to the low quenching rate. In a previous study, Ti–C was added to suppress the growth of such grains. [11]

We examined the relation between the microstructure, observed using FE-EPMA, and the domain structure, observed using a Kerr microscope, for evaluating the effects of hot rolling and the addition of Ti–C on the c-axis orientation and the magnetization process of Nd–Fe–B–Ti–C melt-spun ribbons. This study aims to establish the coercivity mechanism of magnets by observing their magnetic domains.

2. Experimental

A steel subroll was placed on a steel wheel near a quartz tube for hot rolling the melt-spun ribbons immediately after quenching, as in ref 11. Alloys of $Nd_{13}(Fe_{0.95}Ti_{0.05})_{81}B_{5.4}C_{0.6}$ were melt spun and hot rolled at 150 MPa. X-ray diffraction (XRD) patterns were measured on both surfaces of the ribbon. The magnetization curve of the ribbon was obtained parallel and perpendicular to the pressing direction using a vibrating sample magnetometer with a maximum applied field of 33 kOe. The microstructure of the cross section of the ribbon was observed with a FE-EPMA. At the

same spot observed with FE-EPMA, magnetic domains were observed with a Kerr microscope by applying a DC magnetic field up to 14 kOe.

3 Results and discussion

The XRD patterns of both surfaces of the Nd–Fe–B–Ti–C ribbon are shown in Fig. 1. The subroll surface of the ribbon shows reflections from the (004), (006), and (008) planes, observed from the reflections from the c plane of $Nd_2Fe_{14}B$, as shown in Fig. 1(a). The main wheel surface also exhibits reflections from the c plane, as shown in Fig. 1(b). The data suggest that the c axis is oriented normal to the ribbon plane, which is parallel to the hot-rolling pressing direction. The addition of Ti–C has been found to promote the c-axis orientation of the Nd–Fe–B melt-spun ribbon by hot rolling. [4]

Figure 2 shows the magnetization curves of the Nd–Fe–B–Ti–C ribbon. The residual magnetization and coercivity along the perpendicular direction, which is parallel to the hot-rolling pressing direction, improve by the addition of Ti–C, as in ref 11. The coercivity along the perpendicular direction is 10.6 kOe, as shown in Fig. 2. However, anisotropic magnetic properties are not observed in the magnetization curves of the Nd–Fe–B–Ti–C ribbon showing the c-axis orientation in the XRD patterns.

Figure 3 shows a compositional scanning electron microscope (SEM) image and

EPMA elemental maps of Fe, Nd, and Ti for the Nd–Fe–B–Ti–C ribbon. The EPMA elemental maps suggest a uniform elemental distribution. From the compositional SEM image, as shown in Fig. 3(a), the dark contrast area is covered by the bright contrast points. These points coincide with the Nd-enriched and Fe-poor points, as shown in Fig. 3(a), 3(b), and 3(c). The data suggest that the bright and dark contrast areas of the compositional image correspond to the main Nd–Fe–B phase and the Nd-rich grain-boundary phase, respectively. The size of the grains depends on the position along the perpendicular direction, as shown in Fig. 3(a). The grains near the subroll surface are larger than those near the main roll surface because the quenching rate around the subroll surface is lower than that around the main roll surface. The enlarged grains near the subroll surface decrease the coercivity of the ribbon.

Figure 4 shows the Ti distribution observed by FE-EPMA at the enlarged grain of a few tens of μm in size. Although most Ti-enriched points exist at grain boundaries, some are inside the grain, as indicated by the arrow in Fig. 4. The elemental maps of Ti and Fe suggest that the Ti-enriched area coincides with the Fe-poor area, as shown in Fig. 5.

Figure 6 shows domain images of the ribbon when a DC field from +14 kOe to −14 kOe was applied along the perpendicular direction. In these figures, the dark and bright areas

indicate upward and downward magnetization components, respectively. When the DC field was decreased from +14 kOe to +9.5 kOe in the upward direction, the enlarged grain exhibited a dark domain having upward magnetization components, as shown in Fig. 6(a). The data indicate that a single-domain state in the grain was obtained at that field value. When the DC field was decreased to +9.5 kOe, some reversal domains, indicated by the brighter areas, nucleated in the grain, surrounded by the dotted circle shown in Fig. 6(b), and the domain structure changed from the single-domain state to the multidomain state inside the grain. The reversed domains grew when the DC field was changed to −14 kOe.

Figure 7 shows the Ti distribution in the enlarged grain (green colored areas) and the reversal domain at 9.5 kOe (blue colored areas). As shown in the figure, the reversal domains nucleated at the Ti-enriched point inside the grain, surrounded by the dotted circle. The data suggest that the addition of excess Ti promotes the poor distribution of Ti and causes low coercivity.

4 Conclusion

In this study, the relation between the microstructure, observed using FE-EPMA, and the domain structure, observed using a Kerr microscope, was established to evaluate the

effects of hot rolling and the addition of Ti–C on the c-axis orientation and the magnetization of hot-rolled Nd–Fe–B–Ti–C melt-spun ribbons. The addition of Ti–C promotes the c-axis orientation and high coercivity in the Nd–Fe–B melt-spun ribbon. The EPMA elemental maps suggest a uniform elemental distribution. However, an uneven distribution of Ti was observed in an enlarged grain with Ti-enriched points inside the grain. The reversal domains that nucleated at the Ti-enriched point inside the grain are responsible for the low coercivity.

References

[1] Hirosawa S, Nishiuchi T, Nozawa N, Ohkubo T, Hono K, Sepehri-Amin H, Takezawa M, Yamasaki J, Yamanuro S, Tanaka T, Okano M, Sumiyama K. Recent Efforts Toward Rare-Metal-Free Permanent Magnets in Japan. Proceedings of the 21st Workshop on Rare-Earth Permanent Magnets and their Applications, Bled, 2010: 187-192

[2] Sugimoto S, Recent Trend of the Researches for Reducing Dysprosium Usage in a Nd-Fe-B Sintered Magnet. Journal of the Japan Society of Powder and Powder Metallurgy, 2010, 57: 395-400

[3] Sepehri-Amin H, Ohkubo T, Nishiuchi T, Hirosawa S, Hono K. Coercivity

Enhancement of Hydrogenation-Disproportionation-Desorption-Recombination Processed Nd-Fe-B Powders by the Diffusion of Nd-Cu Eutectic Alloys. Scripta Materialia, 2010, 63: 1124-1127

[4] Liu M, Sun Y, Han G B, Yang W, Gao R W. Dependence of Anisotropy and Coercivity on Microstructure in HDDR Nd-Fe-B Magnet Journal of Alloys and Compounds, 2009, 478: 303-307

[5] Li W F, Ohkubo T, Hono K, Nishiuchi T, Hirosawa S. The Role of Grain Boundaries in the Coercivity of Hydrogenation Disproportionation Desorption Recombination Processed Nd-Fe-B Powders. Journal of Applied Physics, 2009, 105: 07A706

[6] Thompson P, Gutfleisch O, Chapman J N, Harris I R. A Comparison of the Micromagnetic and Microstructural Properties of Four NdFeB-Type Materials Processed by the HDDR Route. Journal of Magnetism and Magnetic Materials, 1999, 202: 53-61

[7] Mishra R K, Lee R W. Microstructure, Domain Walls, and Magnetization Reversal in hot-Pressed Nd-Fe-B Magnets. Applied Physics Letters, 1986, 48: 733-735

[8] Lee R W, Brewer E G, Schaffel N. Processing of Neodymium-Iron-Boron Melt-Spun Ribbons to Fully Dense Magnets. IEEE Transactions on Magnetics, 1985, 21: 1958-1963

[9] Kuji T, O'Handley R C, Grant N J. Magnetic Anisotropy of $Nd_{15}Fe_{77}B_8$ Flakes Made by Twin-Roller Quenching. Applied Physics Letters, 1989, 54: 2487-2489

[10] Kuji T, O' Handley R C, Grant N J. Method for Making Polycrystalline Flakes of Magnetic Materials Having Strong Grain Orientation. US Patent, 1991, 5049335

[11] Takezawa M, Nakanishi Y, Morimoto Y, Yamasaki J, Yagi M. Investigation of Easy Axis Orientation of Nd-Fe-B Melt-Spun Ribbons Produced by hot Rolling and Influence of Ti-C Addition. Journal of Applied Physics, 2012, 111: 07A703

Figure captions

Fig. 1 XRD patterns of the $Nd_{13}(Fe_{0.95}Ti_{0.05})_{81}B_{5.4}C_{0.6}$ ribbon: (a) subroll surface and (b) main wheel surface.

Fig. 2 Magnetization curve of the $Nd_{13}(Fe_{0.95}Ti_{0.05})_{81}B_{5.4}C_{0.6}$ ribbon.

Fig. 3 (a) Compositional SEM image and EPMA elemental maps of (b) Fe, (c) Nd, and (d) Ti in the Nd–Fe–B–Ti–C ribbon.

Fig. 4 Optical microscope image and the elemental map of Ti at the enlarged grain.

Fig. 5 EPMA elemental maps of Fe, Nd, B, and Ti at the enlarged grain.

Fig. 6 Domain images of the cross-sectional surface: (a)+14 kOe, (b) +9.5 kOe, (c) +4.0 kOe, (d) 0, (e) −5 kOe, and (f) −13.5 kOe.

Fig. 7 Magnetization reversal area and Ti distribution.

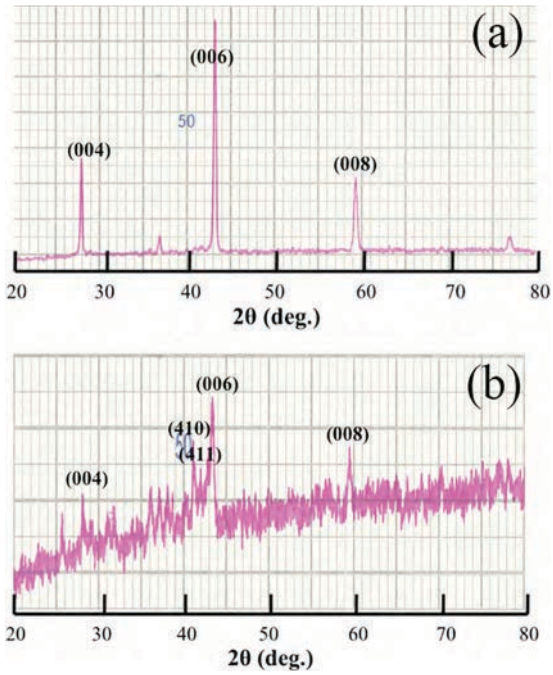
(a)
(006)
(004)
(008)
20
30
40
50
60
70
80
2θ (deg.)
(b)
(006)
(410)
(411)
(008)
(004)
20
30
40
50
60
70
80
2θ (deg.)

FIG1

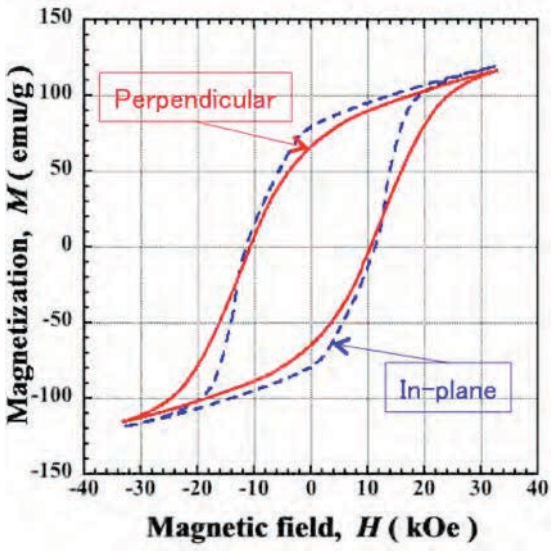
Perpendicular
In-plane
Magnetization, M (emu/g)
Magnetic field, H (kOe)
150
100
50
0
-50
-100
-150
-40
-30
-20
-10
0
10
20
30
40

FIG2

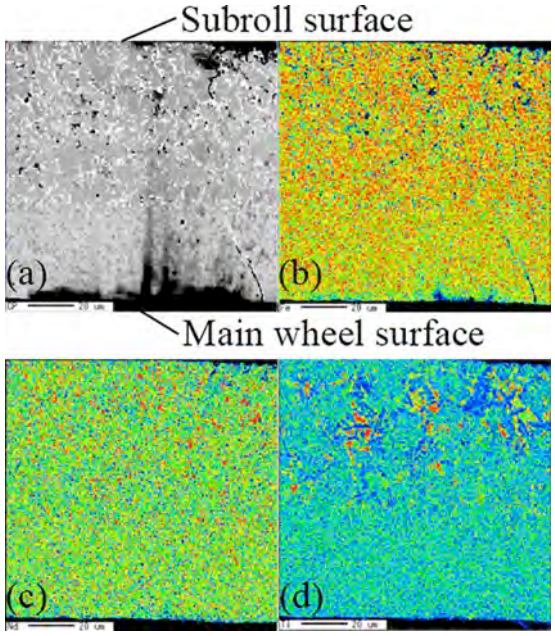

FIG3

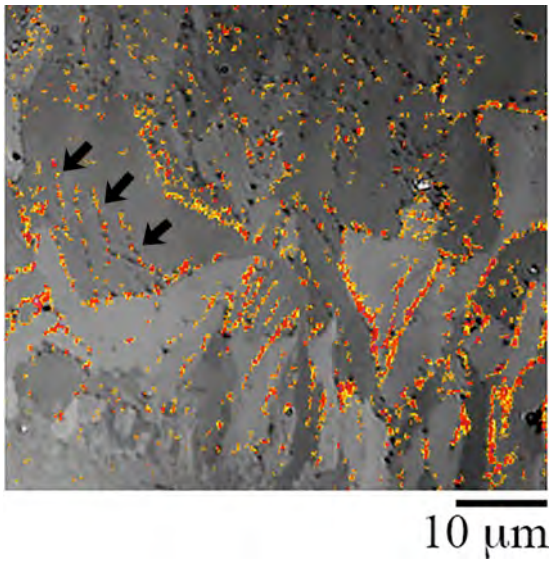

FIG4

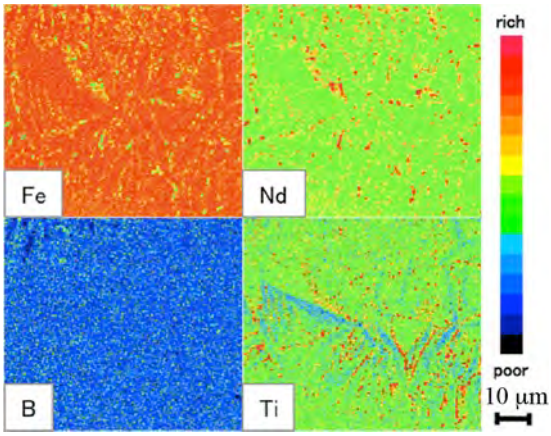

FIG5

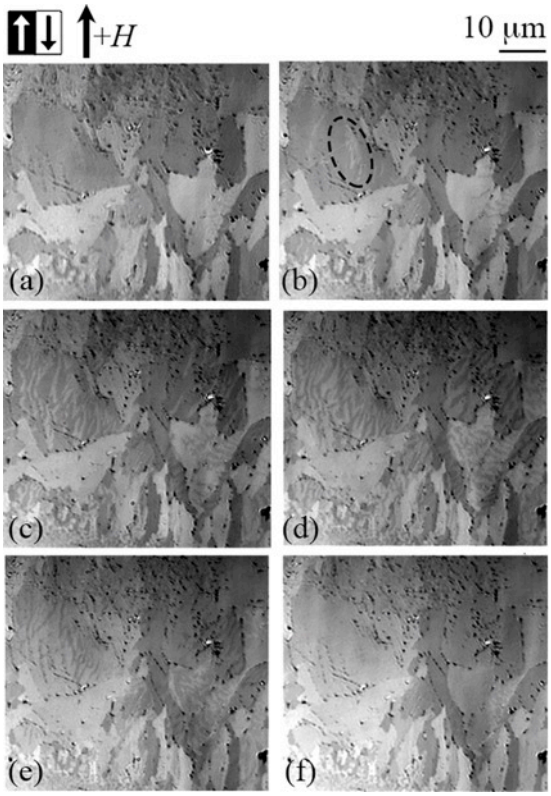

FIG6

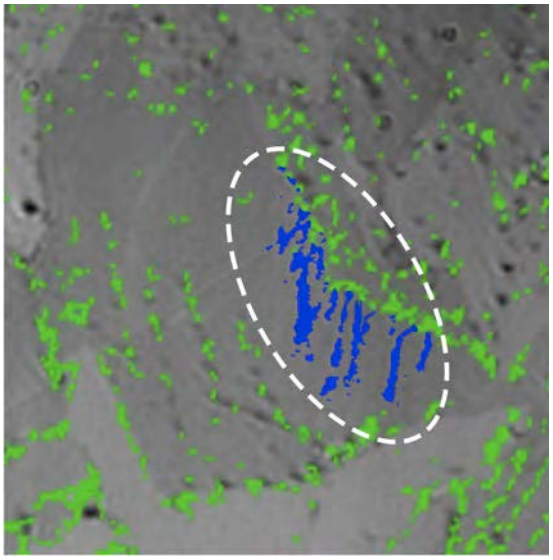

FIG7